Australian Bushfire Emissions Result in Enhanced Polar Stratospheric Ice Clouds

Srinivasan Prasanth[1,2], Narayana Sarma Anand[3], Kudilil Sunilkumar[2], Subin Jose[4], Kenath Arun[1], Sreedharan K. Satheesh[2,5,6], and Krishnaswamy K. Moorthy[5]

[1]Department of Physics and Electronics, Christ University, Bengaluru, Karnataka, India

[2]Centre for Atmospheric and Oceanic Sciences, Indian Institute of Science, Bengaluru, Karnataka, India

[3]School of Earth, Environmental and Sustainability Sciences, Indian Institute of Science Education and Research Thiruvananthapuram, Kerala, India

[4]Department of Physics, Newman College, Thodupuzha, Kerala, India

[5]Divecha Centre for Climate Change, Indian Institute of Science, Bengaluru, Karnataka, India

[6]DST-Centre of Excellence in Climate Change, Indian Institute of Science, Bengaluru, Karnataka, India

Correspondence: Prasanth S. (prasanthphy57@gmail.com)

Abstract

Extreme bushfire events amplify climate change by emitting greenhouse gases and destroying carbon sinks while causing economic damage through property destruction and even fatalities. One such bushfire occurred in Australia during 2019/2020, injecting large amounts of aerosols and gases into the stratosphere and depleting the ozone layer. While previous studies focused on the drivers behind ozone depletion, the bushfire impact on the polar stratospheric clouds (PSC), a paramount factor in ozone depletion, has not been extensively investigated so far. This study focuses on the effects of bushfire aerosols on the dynamics and stratospheric chemistry related to the PSC formation and its pathways. An analysis from Aura's microwave limb sounder revealed enhanced hydrolysis of dinitrogen pentoxide significantly increased nitric acid (HNO_3) in the high-latitude lower stratosphere in early 2020. Using a novel methodology which retrieves formation pathways of PSCs from spaceborne lidar observations, we found that the enhanced HNO_3 condensed on bushfire aerosols, forming 82 % of Liquid Nitric Acid Trihydrate (LNAT), which rapidly converted to 77 % of ice, resulting in an anomalous high areal coverage of ice PSCs. This highlights the primary formation pathways of ice and LNAT and possibly helps us to simulate the PSC formation and denitrification process better in climate models. As tropospheric warming is anticipated to increase the frequency of extreme wildfire events and stratospheric cooling is expected to expand the PSC areal coverage, these findings will contribute significantly to a deeper understanding of the impacts of extreme wildfire events on stratospheric chemistry and PSC dynamics.

Keywords: Aerosols; Australian Bushfire; Formation pathways; Polar Stratospheric Clouds; Stratospheric chemistry

1 Introduction

Southeast Australia, comprising the states of New South Wales and Victoria, faced an extreme bushfire event from September 2019 to February 2020, which is widely recognized as the black summer or Australian New Year (ANY) event and has been extensively studied (Allen et al., 2020; Deb et al., 2020; Schwartz et al., 2020; Chang et al., 2021; Rieger et al., 2021; Tencé et al., 2021, 2022; Heinold et al., 2022; Sellitto et al., 2022;). This catastrophic event injected substantial amounts of aerosols, between 0.4 and 2 Tg, into the southern hemispheric lower stratosphere (Khaykin et al., 2020; Hirsch and Koren, 2021; Heinold et al., 2022; Tencé et al., 2022); which composed of 2.5 % black carbon and 97.5 % organic carbon (Yu et al., 2021). Significant warming of the mid-latitude stratosphere by up to 3.5 K has been reported, which is unparalleled since the 1991 eruption of Mount Pinatubo (Stocker et al., 2021). Additionally, this event led to significant changes in various trace gas species, such as CH_4, CO, CH_3CN, CH_3Cl, HCN, CH_3OH, HCl, HNO_3, H_2O, and $ClONO_2$, particularly in the mid-latitude lower stratosphere (Schwartz et al., 2020; Santee et al., 2022; Wang et al., 2023).

Furthermore, these aerosols provided a surface area for heterogeneous chlorine activation reactions, resulting in the early depletion of HCl and an enhancement of ClO (Santee et al., 2022), and led to additional stratospheric ozone loss (Solomon et al., 2022). Along with these aerosols, liquid Polar Stratospheric Clouds (PSCs) are also known to promote such ozone-depleting heterogeneous reactions (Molina et al., 1993; Carslaw et al., 1994; Ravishankara and Hanson, 1996). Solid PSCs like Nitric Acid Trihydrate (NAT) are known to retard the deactivation process of active halogens like chlorine, bromine, and fluorine through denitrification and thereby contribute to prolonged ozone depletion (Hoyle et al., 2013). Ansmann et al. (2022) reported that the bushfire aerosols from the black summer event have influenced the PSCs by increasing their surface area and particle number concentration. Wang et al. (2023) reported an increased stratospheric chlorine activation on the bushfire aerosols and PSCs. However, previous studies have not extensively investigated the influence of the black summer event on the PSC dynamics, specifically the formation pathways. It is paramount to understand the influence of extreme events like the black summer event on PSC dynamics for two main reasons:

(i) The frequency of extreme wildfire events is projected to increase due to global warming (Mansoor et al., 2022), resulting in more injection of aerosols into the stratosphere, which could enhance the PSC area coverage.

(ii) Stratospheric cooling is anticipated to further expand the PSC coverage, resulting in more surface area density for chlorine activation reactions and thus more ozone depletion (Robrecht et al., 2019).

Under the above backdrop, using multi-satellite measurements and reanalysis data, this study aims to investigate the anomalies in stratospheric chemistry and PSC dynamics caused by the black summer event.

The data and methodology used in this study are detailed in Sect. 2. The results and their discussion are given in Sect. 3 and the study is concluded in Sect. 4.

2 Data and Methodology

2.1 Satellite data

Ozone Monitoring Profiler Suite (OMPS) on board Suomi NPP and NOAA-20 satellites measures atmospheric O_3 and aerosols using limb viewing techniques. We have used OMPS level 2 version 2.0 product which provides aerosol extinction coefficient at 745 nm wavelength, with a horizontal resolution of 125 km × 2 km and a vertical resolution of 1.8 km (https://disc.gsfc.nasa.gov/datasets/OMPS_NPP_LP_L2_AER_DAILY_2/summary; Taha et al., 2021).

Microwave Limb Sounder (MLS) aboard the Aura satellite provides the trace gases mixing ratio by measuring limb emission spectra through a Fourier Transform Spectrometer (FTS). The MLS Level 2, version 5.0 daily HNO_3 and H_2O mixing ratio are used (https://mls.jpl.nasa.gov/eos-aura-mls/data-products; Waters et al., 2006). Atmospheric Chemistry Experiment-FTS (ACE-FTS) onboard SciSat satellite provides trace gases mixing ratio by measuring limb absorption spectra and level 2, version 4.0 daily HF, H_2O, HNO_3, N_2O_5 mixing ratio (https://www.frdr-dfdr.ca/repo/dataset/c75d2c49-0def-49e5-9c69-5e74c824dc6c; Bernath et al., 2020) are used in the present study.

Cloud-Aerosol Lidar with Orthogonal Polarization (CALIOP) onboard the Cloud-Aerosol Lidar and Infrared Pathfinder Satellite Observations (CALIPSO) satellite probes the vertical distribution of aerosols and clouds. The PSCs are detected as those measurements with a relatively larger extinction coefficient than the background aerosol extinction coefficient (Pitts et al., 2007). It classifies the detected PSCs through perpendicular attenuated backscatter and total scattering ratio (ratio between the total attenuated backscatter to the molecular backscatter) into five categories: Supercooled Ternary Solution (STS ≡ $H_2SO_4.HNO_3.H_2O$), Liquid Nitric Acid Trihydrate (LNAT ≡ $HNO_3.3H_2O$, a mixture of liquid STS and solid NAT with low number density of 10^{-2} cm^{-3}), ENAT (Enhanced NAT, with high number density of 10^{-1} cm^{-3}), Ice (Water ice ≡ H_2O), and Mountain Wave Ice (MWI ≡ H_2O, caused by gravity waves). The total areal coverage of the PSCs such as LNAT, STS, Ice, ENAT, and MWI contributes to 48 %, 24.7 %, 21.4 %, 5.8 %, and 0.1 % respectively (Pitts et al., 2018). In this study, CALIPSO PSC Level 2, version 2.0 is used (https://asdc.larc.nasa.gov/project/CALIPSO/CAL_LID_L2_PSCMask-Standard-V2-00_V2-00; Pitts et al., 2007; 2009; 2013), which provides PSC information at a spatial resolution of 180 m (vertical) × 5 km (horizontal). The PSC areal coverage is estimated as described in Pitts et al. (2009).

European Centre for Medium-Range Weather Forecasts Reanalysis fifth generation (ERA-5) reanalysis provides meteorological data with a spatial resolution of 0.25° × 0.25° and a temporal resolution of 1 hour at 37 pressure levels (1000 to 1 hPa). We have used the hourly meridional and zonal velocity from June 2020 to July 2020 (https://cds.climate.copernicus.eu/cdsapp#!/dataset/reanalysis-era5-pressure-levels?tab=overview; Hersbach et al., 2020).

2.2 Anomaly estimation

Anomalies (Δ) in aerosol extinction coefficient (k_{ext} at 745 nm), mixing ratios of H_2O, and HNO_3, and PSC properties are estimated following Eq. (1):

$$\Delta X = X_{2020} - \bar{X} \qquad (1)$$

where 'ΔX' is a daily anomaly of quantity 'X', 'X_{2020}' is the daily mean in 2020, and '$\bar{X}$' is the daily background mean. The background mean values of H_2O and HNO_3 mixing ratio and PSC properties are constructed by averaging the daily values during the period 2009 to 2019 while for k_{ext}, the period is 2012 to 2019 [excluding the year 2015, to avoid the effects of the Calbuco volcanic eruption (Zhu et al., 2018)]. The standardized anomaly (Z) is estimated following Eq. (2):

$$Z_X = \frac{\Delta X}{\sigma_X} \tag{2}$$

where 'σ_X' is the standard deviation of the parameter 'X'.

2.3 Retrieval of formation pathways
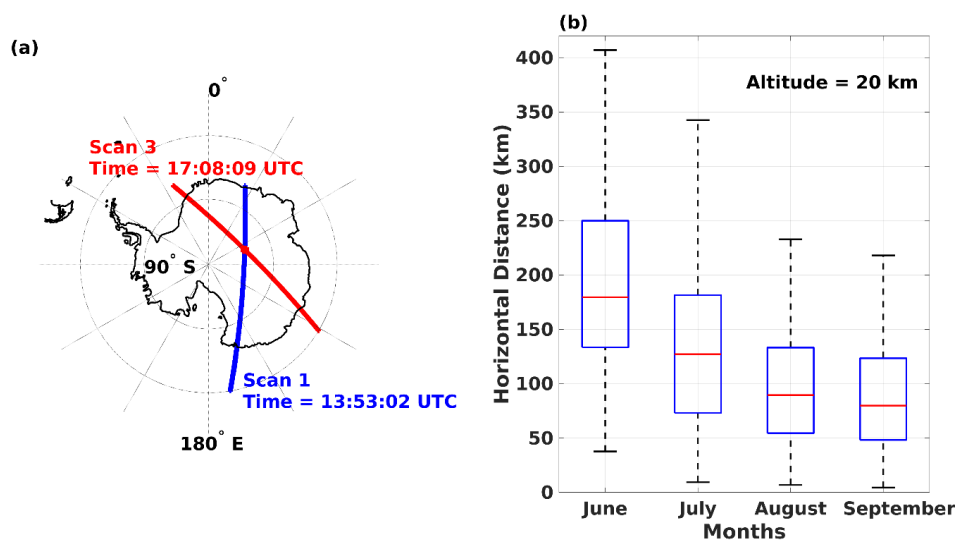
Figure 1: (a) Intersection of two CALIPSO scan tracks: Scan 1 (blue line) and Scan 3 (red line) during 01/08/2020 and (b) Boxplot showing the simulated horizontal distance traveled by air parcels for 240 minutes starting at 00:00 (hour: minutes) at an altitude of 20 km during June, July, August, and September of 2020. In the boxplot, the redline marks the median distance, the horizontal blue lines below and above the median mark the first and third quartile respectively, and the lower and uppermost black lines mark the minimum and maximum distance traveled by the air parcels.

CALIPSO provides PSC composition derived from the backscattered signal, but it does not carry information about the formation pathways of these PSCs. Previous studies retrieved the PSC formation pathways from CALIPSO (Nakajima et al., 2016) and aircraft campaigns (Voigt et al., 2018) using Lagrangian trajectory analysis but were limited to a few days. However, the methodology they employed did not provide a relative percentage contribution of various formation pathways of PSCs. We have developed a new methodology to address this limitation. The CALIPSO orbits the Earth ~15 times per day with an orbit period of ~100 minutes. These scan tracks periodically intersect at high-latitude regions (an example is given in Fig. 1a). The intersection points provide a unique opportunity to measure the PSC composition at certain intervals of time. In this study, we choose the intersection between the scan 'n' and scan '(n+2)' which usually occurs at latitude ~-80°. The time interval

between these two scans is ~200 minutes. Though we have a measurement of the PSC composition at the same location with a periodic time interval, the air parcel tends to move vertically and horizontally. Hence, it is vital to find the distance traveled by air parcels in the given 200 minutes. The vertical velocity of the air parcel at the lower stratosphere is extremely low of order of 0.001 m s^{-1} (Hamill and McMaster, 1984). But horizontal velocity varies according to the prevailing meteorological condition modulated by the polar vortex.

To find the horizontal distance traveled by the air parcels, we utilized a trajectory module from the Chemical Lagrangian Model of the Stratosphere (CLaMS) where the ERA5 hourly meteorological dataset is provided as an input. For the simulation, the initial location of the air parcels is considered to be at latitude -80°, time 00:00 UTC (hh: mm), longitude between 0° and 360° at an interval of 45° and altitude of 20 km. The air parcels are allowed to travel for the next 4 hours (240 mins) in the trajectory module. Though the requirement is to measure the horizontal distance traveled by air parcels in 200 minutes, we run the trajectory module on an hourly scale to reduce the computational cost. Hence, the monthly statistics of the distance traveled by the air parcels in 240 minutes, starting from the initial location, are shown in Fig. 1b.
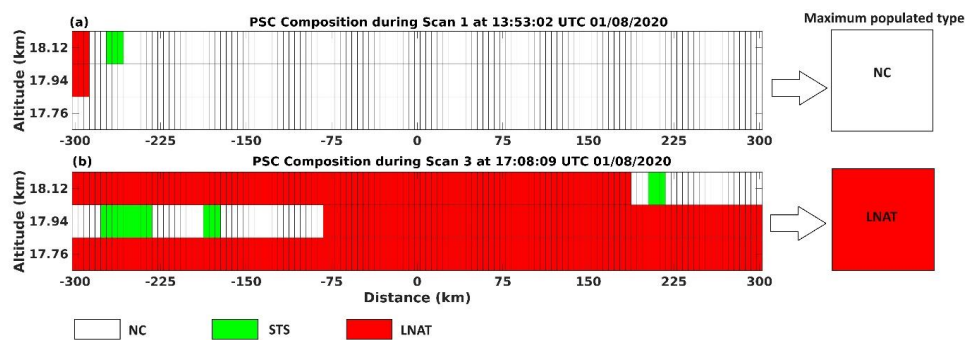
Figure 2: Observed CALIPSO PSC composition during 01/08/2020 at (a) Scan 1 and (b) Scan 3. The '0 km' in the x-axis marks the intersection of the two scan tracks. 'NC', 'LNAT', and 'STS' stand for No Cloud (white), Liquid Nitric Acid Trihydrate (red), and Supercooled Ternary Solution (green).

Based on the trajectory results, it is found that the monthly mean distance traveled by the air parcels is within 300 km. Hence, around the intersection, profiles falling within a 300 km radius and three consecutive vertical levels (i.e., 540 m) are chosen, as shown in Fig. 2. The maximum populated PSC within the chosen boundary is assumed to be the PSC of the air parcel. This reclassification reduces the noise further. The transition in the maximum populated PSC type during the two scans provides vital information about the PSC formation pathways. In CALIPSO PSC Version 2.0, statistical threshold values of perpendicular attenuated backscatter ($\beta_\perp$) and total scattering ratio (R_{532}) are used to classify the PSC composition (Pitts et al., 2009). Here, the perpendicular attenuated backscatter refers to the perpendicular component (i.e., polarization perpendicular to the emitted lidar signal) of the attenuated backscatter signal from the particulate and the total scattering ratio is the ratio between the total particulate backscatter and molecular backscatter. For example, the particle is classified as enhanced NAT PSC if it's $2 < R_{532} < 5$ and $\beta_\perp > 2 \times 10^{-5}$ km^{-1} sr^{-1}, as ice PSC if it's $2.75 < R_{532} < 50$ and $\beta_\perp >\sim 1.55 \times 10^{-5}$

km^{-1} sr^{-1} and STS PSC if it's β⊥ < ~1.55×10^{-5} km^{-1} sr^{-1} (Pitts et al., 2009, 2018). Similarly, the other types of PSCs are classified based on empirically found threshold values. More details can be found in Pitts et al. (2009).

155 We choose PSCs whose optical properties are far away from these thresholds (i.e., more than one standard deviation with respect to the threshold value). Through this, we ensure that only grids which exhibited drastic change in PSC optical properties during the 200 minutes are considered for the retrieval of PSC formation pathways. It should be noted that as these intersections occur at the latitude of ~-80°, the retrieved formation pathways correspond to the interior of the polar vortex. As such, they cannot be considered representative of all

160 PSC formations which occur outside the polar vortex.

The CALIPSO PSC composition observed on 01/08/2020 in Scan 1 and Scan 3 are shown in Fig. 2. The horizontal and vertical boundaries are selected as described above. During Scan 1, No Cloud (NC) is the maximum populated PSC type (NC refers to the presence of no clouds as observed by CALIPSO but may contain stratospheric aerosols/sub-visible PSC/NAT rock (Tritscher et al., 2021)). Hence, all grids within this boundary are labeled as

165 'NC. During scan 3, as LNAT is the maximum populated PSC type, it is traced that "NC" turned into "LNAT" in the given ~200 minutes. Similarly, all possible formation pathways of both ice and LNAT are retrieved during each successful intersection point. This technique helps us to narrow down the possible formation pathways. However, it is difficult to uniquely conclude the formation pathways using CALIPSO PSC information only. Because, as discussed earlier, 'NC' refers to the air parcel containing either stratospheric aerosols or large NAT

170 rock, whose optical properties are below the CALIPSO detection threshold. If the same air parcel became populated with 'LNAT' after a certain time, it could imply that it either formed through nucleation on stratospheric aerosols aided by decreased temperature or evaporation of large NAT rock aided by increased temperature such that its size now falls within CALIPSO detection thresholds. Hence, to conclude which formation pathway is responsible for the specific PSC formation, it is essential to consider the corresponding change in temperature and

175 gaseous species also, as described in the next section.

2.4 Thermodynamic Analysis of PSC Formation Pathways

The change in air temperature and gas-phase HNO$_3$ mixing ratio offer valuable insight into potential PSC formation pathways, as described in Sect. 2.3, we accounted for changes in these parameters when retrieving the PSC formation pathways (Nakajima et al., 2016). Furthermore, each formation pathway occurs at a specific

180 temperature, which is conventionally viewed in the 'T-T$_{ice}$' temperature coordinate (Lambert et al., 2012; Pitts et al., 2013). Here 'T' is the ambient air temperature and 'T$_{ice}$' is the frost point (the temperature at which the air parcel saturates with water vapor, leading to ice formation). The estimation of 'T$_{ice}$' follows the parameterization described in Murphy and Koop (2005). The change in air temperature 'ΔT', and gas-phase nitric acid 'ΔHNO$_3$' are estimated following Eqs. (3) and (4) respectively.

185
$$\Delta T = T_n - T_{n+2} \qquad (3)$$

$$\Delta HNO_3 = HNO_{3_n} - HNO_{3_{n+2}} \qquad (4)$$

where T_n and HNO_{3_n} respectively represent the temperature and HNO$_3$ mixing ratio of the air parcel during the scan 'n'. The temperature and HNO$_3$ are obtained from MLS and MERRA-2 (provided along with CALIPSO PSC v2.0 product) respectively. For reliable results, the estimated ΔT and ΔHNO$_3$ (using Eqs. 3 and 4) should be

190 statistically significant such that their magnitude should be higher than their respective measurement uncertainties. The measurement uncertainty (represented by σ) in temperature and HNO$_3$ is 0.5 K (Graham et al., 2019) and 0.6 ppbv (Lambert et al., 2016) respectively. Hence, the combined uncertainty in ΔT and ΔHNO$_3$ are estimated following the summation in quadrature rule (Bell, 2001) as written in Eq. (5):

$$\sigma(\Delta x) = \sqrt{2\sigma(x)^2} \qquad (5)$$

195 Where '$\sigma(\Delta x)$' represents the uncertainty in Δx, and 'x' represents the HNO$_3$ mixing ratio or T. Similarly, the uncertainty in 'T-T$_{ice}$' is estimated following Eq. (6):

$$\sigma(T - T_{ice}) = \sqrt{(\sigma(T))^2 + (\sigma(T_{ice}))^2} \qquad (6)$$

Where σ(T$_{ice}$) is the uncertainty in T$_{ice}$ which is taken as 0.5 K (Lambert et al., 2016). To ensure the reliability of the results, we are excluding values of ΔT, ΔHNO$_3$, and T-T$_{ice}$ falling within the respective uncertainty limits
200 σ(T), σ(HNO$_3$), and σ(T-T$_{ice}$).

3 Results and discussions

3.1 Increased aerosol loading in the lower stratosphere
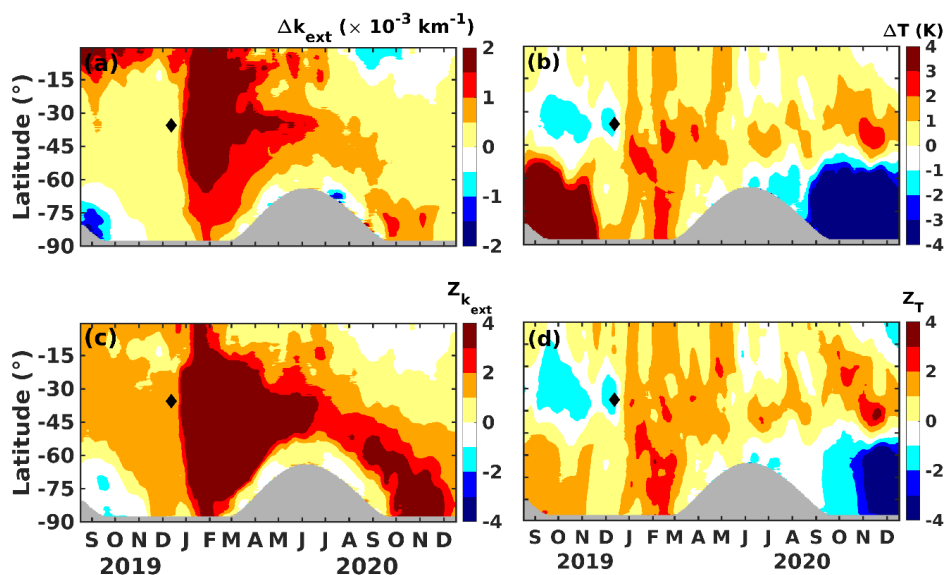
Figure 3: Daily zonal mean anomaly (Δ) in OMPS (a) k$_{ext}$ at 745 nm, (b) temperature, and standardized anomaly
205 *(Z) of (c) k$_{ext}$ at 745 nm and (d) temperature at the altitude of 15 km between September 2019 and December 2020 are shown. The grey-shaded region corresponds to no data. The x-ticks mark the middle of each month. The black diamond in each plot marks the black summer event.*

An anomaly in aerosol extinction coefficient (k$_{ext}$) at 745 nm and temperature along with their corresponding standardized anomalies at the altitude of 15 km are shown in Fig. 3. A notable positive anomaly of k$_{ext}$ in mid-
210 latitude since early January 2020 is attributable to the increased aerosol loading caused by the black summer event

(Fig. 3a). The anomaly in k_{ext} exceeded three standard deviations (Fig. 3c) and warmed the lower stratosphere by 2 K owing to the radiative heating (Rieger et al., 2021), which is readily seen in Fig. 3b. By February 2020, these aerosols have been transported to high latitudes where PSC usually forms in the subsequent Austral winter. As stratospheric aerosols act as nuclei for PSC, it is likely that these aerosols also influenced the PSC dynamics

215 during this period. Since April 2020, a negative anomaly of k_{ext} has been observed at the latitude ~-80°, which is attributed to the nucleation of PSC on these aerosols (Zhu et al., 2018). The k_{ext} increased again at high latitudes in October and November 2020 which is due to the re-release of the captured aerosols by the PSC, upon evaporation of the corresponding gas species (Toon et al., 1989; Schwarzenböck et al., 2001; Rex et al., 2004; Hoyle et al., 2013). Previous studies reported additional ozone loss during the same period (Ansmann et al., 2022;

220 Ohneiser et al., 2022). Despite the abundant aerosol loading, strong cooling of more than 3 K is observed at high latitude regions from September to December 2020 (Fig. 3b). This suggests that the radiative cooling caused by the additional ozone loss (Fig. S1) has surpassed the radiative heating by the increased aerosol loading, in agreement with Rex et al., (2004). Before the black summer event, intense warming exceeding 5 K was observed at the high latitude of the lower stratosphere from September to November 2019, which was attributed to the

225 minor sudden stratospheric warming event (Liu et al., 2022).
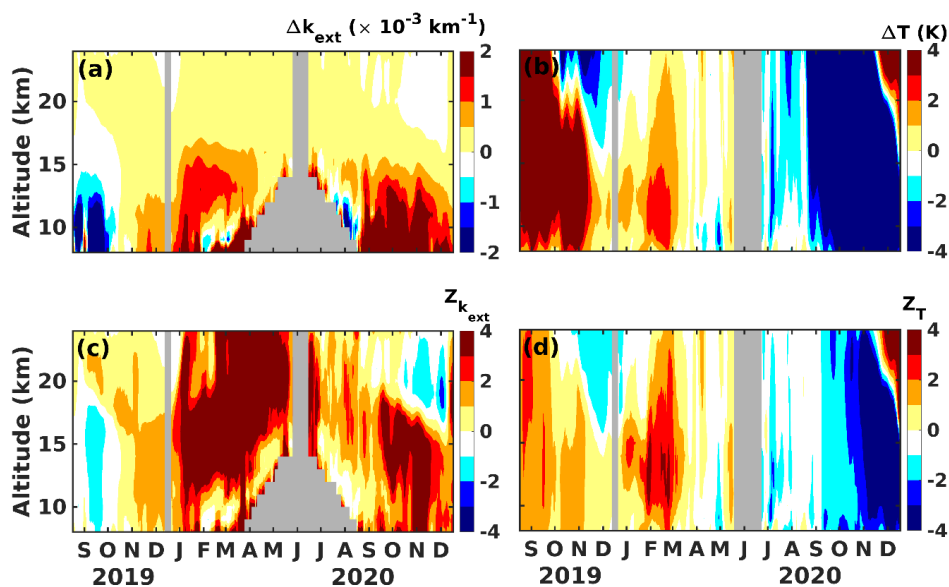
Figure 4: Daily vertical anomaly (Δ) in OMPS (a) k_{ext} at 745 nm, (b) temperature, and standardized anomaly (Z) of (c) k_{ext} at 745 nm and (d) temperature averaged between latitude -60° and -90° from September 2019 to December 2020 are shown. The grey-shaded region corresponds to no data. The x-ticks mark the middle of each
230 *month. The black diamond in each plot marks the black summer event.*

The vertical profiles of anomaly and standardized anomaly (Z) of k_{ext} and temperature are shown in Fig. 4. Significant aerosol loading is observed in Fig. 4a between the altitudes of 10 to 25 km from January to June 2020. The continuous increase in Zk_{ext} since January 2020, to an even higher altitude (Fig. 4c), is attributed to the self-lofting mechanism (Khaykin et al., 2020). Like Fig. 3, the positive anomaly in k_{ext} in the lower stratosphere from

235 October to December 2020 surpassed the anomaly observed during early 2020. The major type of aerosol emitted

during the black summer is organic carbon (Yu et al., 2021), which is hydrophilic in nature. The increased k_{ext} could hence be due to the exposure of these aerosols in the low temperatures during the winter where condensation of water vapor resulted in the growth of the aerosols, increasing its size and light extinction further. In addition, the transport of more bushfire aerosols from mid to high latitude regions could be another cause of the observed increase in k_{ext}. The descending pattern as observed in Zk_{ext} (Fig. 4c) from August to December 2020 could be due to the result of mesospheric air, as explained by Kessenich et al. (2023).

These observations reveal high aerosol loading in the lower stratosphere of the high latitudes after the black summer event. It can increase the surface area availability for heterogeneous chemical reactions and potentially modify the stratospheric chemistry itself. For a comprehensive understanding of the impact of the black summer event on the PSC dynamics, we explore the changes in key constituent gases of PSCs in the next section.

3.2 Enhanced HNO₃ and H₂O in the lower stratosphere

The anomalies in MLS HNO_3 and H_2O mixing ratios along with their corresponding standardized anomalies averaged between latitudes -60° and -90° are shown in Fig. 5. An elevated level of HNO_3 mixing ratio has been observed between 20 to 30 km altitude since February 2020 and peaked by 1.5 ppb over the background value by April 2020 (Fig. 5a). This surge exceeded two standard deviations and remained significant till June 2020 at the altitude of 20 km (Fig. 5c). Similarly, an increase in the H_2O mixing ratio is observed at slightly lower altitudes (between 15 to 20 km) since mid-January 2020 (Fig. 5b), which exceeded more than one standard deviation (the cause of this anomalous increase is discussed in Sect. 3.3). As both HNO_3 and H_2O are principal constituents of the PSCs (Tritscher et al., 2021), the near-simultaneous decrease of them along with k_{ext} (Fig. 4a) during Austral winter suggests that these species condensed on the bushfire aerosols and thus likely converted into PSCs.
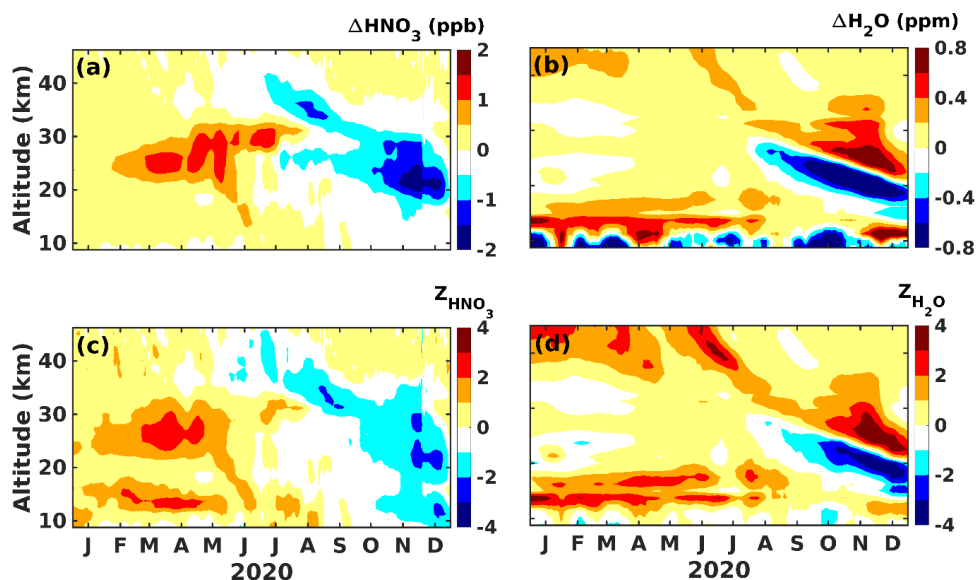
Figure 5: Anomaly in (a) HNO₃ and (b) H₂O mixing ratio, and standardized anomaly of (c) HNO₃ and (d) H₂O mixing ratio, averaged between latitudes -60° and -90° during 2020. The x-ticks mark the middle of each month.

Unlike HNO_3, abundant water vapor is detected in the upper stratosphere (above 40 km) (Fig. 5b and d) from
January to April 2020. Since there is no evidence that the smoke plume from the black summer event has reached
such altitudes, we believe that the moist upper stratosphere is not associated with the black summer event.
Typically, the upper stratospheric water vapor is produced through the oxidation of methane CH_4 (Brewer, 1949;
Fueglistaler et al., 2009) and directly injected from the tropical tropopause layer through deep convection
(Schoeberl et al., 2018). This water vapor is further transported from low to high latitudes through a deep branch
(present at the upper and middle stratosphere) and a shallow branch (present just above tropopause) of the Brewer-
Dobson circulation (Butchart, 2014). The descent of water vapor from the upper stratosphere to the lower
stratosphere during 2020 in Fig. 5b suggests that these water vapors are carried by the deep branch of the Brewer-
Dobson circulation and resulted in a strong positive H_2O anomaly from September to December 2020 within the
altitudes 30 to 25 km. A strong negative anomaly in both HNO_3 and H_2O can be observed below this layer, which
could be due to the prolonged polar vortex during this period separating the mid and high-latitude air mass, thereby
preventing further mixing. To understand whether the cause of these anomalies during early 2020 was due to
dynamical (i.e. due to change in transportation) or chemical (i.e., due to chemical reaction) processes, tracer-trace
correlation analysis was carried out and the results are discussed in the next section.

3.3 Tracer-Tracer Correlation Analysis

The Tracer-Tracer correlation analysis technique is used to diagnose whether a change in atmospheric gas
concentration is driven by chemical reactions or transportation (such as convection or advection. The idea behind
this technique is that chemically active and long-lived tracer (i.e., chemically inert) gas should exhibit the same
order of change if the cause is transport-related (Müller et al., 1996, 1997). If a chemically active gas
increases/decreases with no change in long-lived tracer gas, that change is attributed to the chemical reaction. In
this technique, a linear regression between the long-lived tracer gas and the chemically active gas is performed.
A deviation from the regression line indicates the chemical production of the chemically active gases. For our
analysis, hydrofluoric acid (HF) was chosen as the long-lived tracer gas, as it is chemically inert in the stratosphere
(Wang et al., 2023).
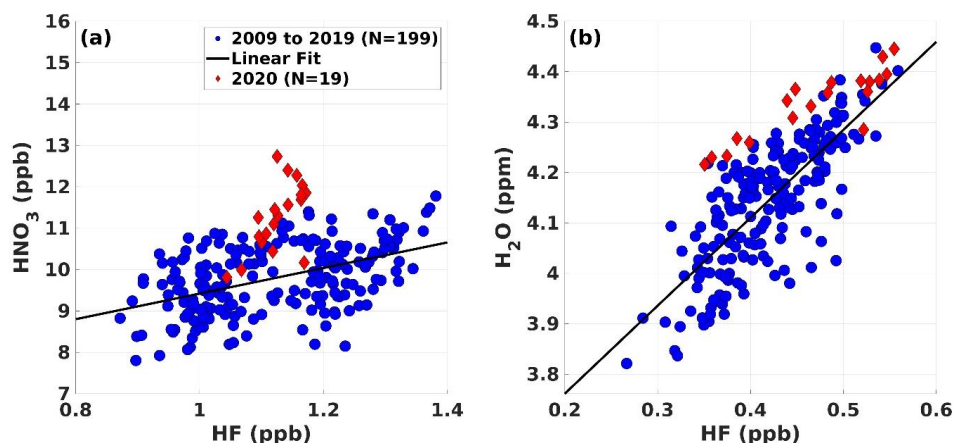
285   *Figure 6: Tracer-Trace correlation between ACE-FTS (a) HNO₃ and HF at the altitude of 25 km, and (b) H₂O vs HF at the altitude of 17 km. The blue circle and red diamond correspond respectively to the periods March 2009– 2019 and March 2020, and the solid black line is a linear fit. Here, 'N' is the number of data points used for regression analysis for both subplots.*

The Atmospheric Chemistry Experiment - Fourier Transform Spectrometer (ACE-FTS) obtained HF is regressed

290   against HNO₃ and H₂O at altitudes of 25 km and 17 km respectively during March 2020 (Fig. 6). The results suggested that the HNO₃ was produced through a chemical process as the data corresponding to March 2020 (red diamond in Fig. 6a) deviate much from the linear fit (black line). In contrast, increased H₂O is transport-related as the data are close to the linear fit (Fig. 6b) and likely carried to the lower stratosphere by the smoke plumes from the black summer event (Schwartz et al., 2020). The production of HNO₃ in the lower stratosphere is

295   governed by the heterogeneous chemical reactions in dinitrogen pentoxide (N_2O_5) hydrolysis, which can be written as (Zhang et al., 1995):

$$N_2O_5 + H_2O \rightarrow 2HNO_3 \tag{R1}$$

We noticed coinciding depletion in ACE-FTS N_2O_5 at the altitude of 25 km during the same period (Fig. 7a) and performed a similar tracer-tracer correlation analysis for N_2O_5 (Fig. S2). The result indicates that N_2O_5 is

300   chemically depleted in the lower stratosphere, suggesting the possible role of the N_2O_5 hydrolysis process. In general, the stratospheric background aerosols provide a surface for H_2O to condense and gas-phase N_2O_5 reacts with it to form HNO_3. To confirm the involvement of the N_2O_5 hydrolysis process, H_2O, N_2O_5, and HNO_3 from ACE-FTS, and k_{ext} at 745 nm from OMPS at 25 km altitude from February to May 2020 are analyzed and shown in Fig. 7.
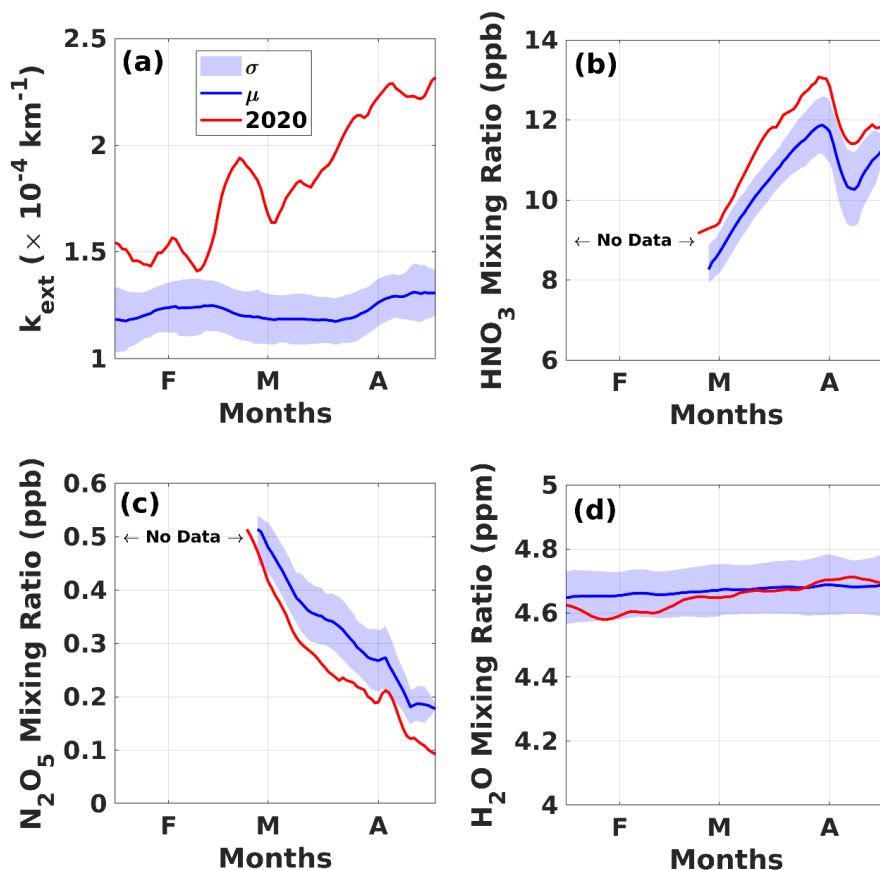
Figure 7: OMPS obtained (a) k_{ext} at 745 nm, and ACE-FTS obtained (b) HNO_3, (c) N_2O_5, and (d) H_2O mixing ratio at the altitude 25 km averaged between the latitude band -60° to -90°. Here, 'σ' represents the standard deviation with respect to the background mean 'μ'. The x-ticks mark the middle of each month.

The background mean of k_{ext} remains ~1.25×10^{-4} km^{-1} between February to May (Fig. 7a). But since early 2020, k_{ext} gradually increased to peak at 2.4×10^{-4} km^{-1} by April 2020. This increasing trend of k_{ext} could be attributed to the coupled effect of the transportation of even more bushfire aerosols from mid to high latitude as days passes and aerosol aging, where bushfire aerosols mixed with stratospheric sulfate aerosols result in an increased size and extinction coefficient (Li et al., 2021; Ohneiser et al., 2022). The simultaneous production and depletion of HNO_3 and N_2O_5 exceeded the respective standard deviations and substantiated that HNO_3 is produced through N_2O_5 hydrolysis (Fig. 7b and c).

During Austral winter, due to the continued lack of solar radiation, the temperature of the polar region decreases by less than 195 K, which results in the condensation of these trace gases, forming PSC. The near-simultaneous decrease in aerosol loading (as discussed in Sect. 3.2), HNO_3, and H_2O at the lower stratosphere during the early winter of 2020 suggests that these changes possibly affected the PSC formation. A comprehensive investigation of PSC dynamics was carried out using CALIPSO measurements and discussed in the next section.

3.4. Impact of the black summer event on the PSC areal coverage during 2020
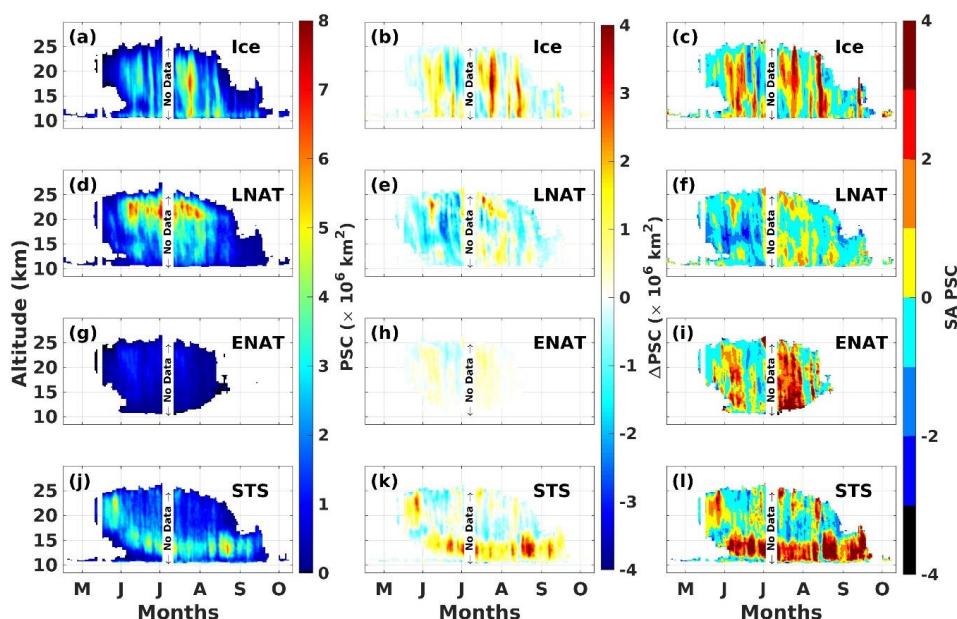
Figure 8: CALIPSO Antarctic PSC areal coverage monthly mean (left column, panels a, d, g, and j), anomaly (middle column, panels b, e, h, and k), and standardized anomaly (right column, panels c, f, i, and l) for the year 2020.

The Antarctic PSC areal coverage for the year 2020, and corresponding anomalies and standardized anomalies are estimated (as described in the methodology Sect. 2.3) and are shown in Fig. 8. CALIPSO detected the PSC from late May onwards (Fig. 8) but the depletion in HNO_3 has been apparent since mid-April itself (Fig. 7c). This could be attributed to the sub-visible PSCs whose optical properties are below the detection threshold of the CALIPSO (Lambert et al., 2012; 2016). Peak positive anomaly of up to 4×10^6 km^2 is exhibited by ice at the altitude between 15 km and 20 km during the second week of August 2020. Followed by ice, the Supercooled Ternary Solution (STS) exhibited a high positive anomaly, which peaked up to 3.5×10^6 km^2 at an altitude between 12 km and 15 km during early September 2020. Since the STS is always in the liquid state and has a relatively higher surface area density than the solid PSCs, the amplification in the STS areal coverage can potentially promote the heterogeneous chlorine activation reaction and lead to additional ozone loss (Molina et al., 1993; Carslaw et al., 1994; Ravishankara and Hanson, 1996). Similarly, an increase in Enhanced Nitric Acid Trihydrate (ENAT) areal coverage is observed but its contribution to the total PSC areal coverage is negligible. It is evident from Fig. 8 that the positive anomalies in the areal coverage of PSCs like ice, STS, and ENAT exceeded three standard deviations with respect to the background mean. The increase in HNO_3 containing PSCs: STS and ENAT can be attributed to the increased surface area provided by the bushfire aerosols and the production of HNO_3 through the N_2O_5 hydrolysis process. In contrast, the areal coverage of another HNO_3 containing PSC, i.e., Liquid Nitric Acid Trihydrate (LNAT), exhibited strong negative anomalies (Fig. 8 e, f).

For instance, during June and July 2020, areal coverage of LNAT decreased significantly, leading to a negative anomaly of up to 2.5×10^6 km^2, which is more than two standard deviations from the background mean (Fig. 8 e,

345 f). During the same period, a significant increase in ice areal coverage of up to 2×10^6 km^2 is observed, exceeding two standard deviations (Fig. 8 b, c). Similar simultaneous positive and negative anomalies in ice and LNAT are observed during August 2020 as well. As NAT can serve as efficient nuclei for ice formation (Hoyle et al., 2013), a possible explanation for this observation could be the heterogeneous nucleation process of ice on existing NAT PSC. To verify this hypothesis, we developed a novel methodology which retrieves the PSC formation pathways,

350 and the results are discussed in the next section.

3.5. Formation pathways of LNAT and Ice PSC

The PSC formation pathways are retrieved from the CALIPSO PSC measurements, as described in Sect. 2.3, during the Austral winter of 2020, and are shown in Fig. 9.
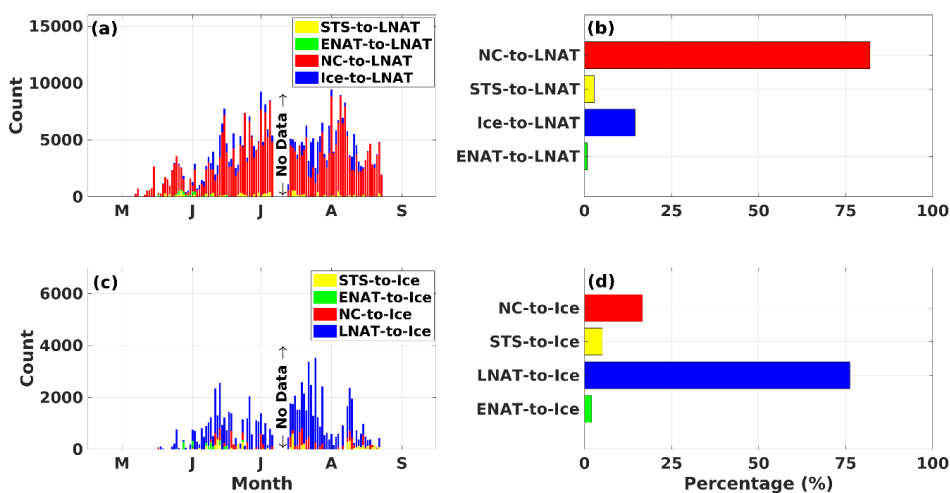
355 *Figure 9: (a) Formation pathways of LNAT, (b) percentage contribution of LNAT formation pathways, (c) Formation pathways of ice, and (d) percentage contribution of ice formation pathways, for the year 2020. The 'Count' in the y-axis of panels (a) and (c) represents the number of CALIPSO grids or pixels exhibiting transition in PSC composition. The x-ticks mark the middle of each month.*

3.5.1 LNAT formation pathways

360 The change in air temperature (ΔT), HNO$_3$ (ΔHNO$_3$), and temperature (T-T$_{ice}$) at which transition in PSC composition is observed are shown respectively in Fig. 10 and Fig. 11. The negative and positive values of 'ΔT' ('ΔHNO$_3$') indicate the cooling (uptake) and warming (release) of the air parcels (gas-phase HNO$_3$). As 'ΔT' and 'ΔHNO$_3$' exhibit skewed distributions (not shown here), their median values are chosen to represent the average (Huff, 2023).

365
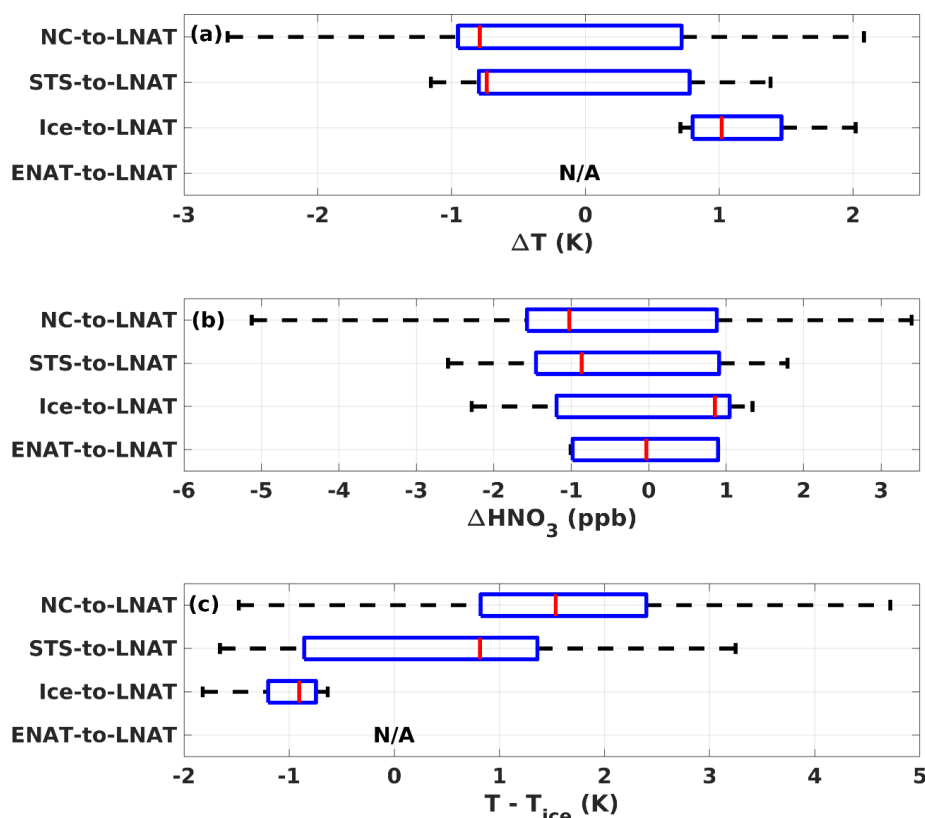
Figure 10: Observed change in (a) temperature (ΔT) and (b) HNO₃ (ΔHNO₃) of the air parcels in which various formation pathways leading to LNAT formation are shown. The temperature at which LNAT forms is shown on the T-T_{ice} temperature coordinate in panel (c). 'N/A' represents no availability of data. In the boxplot, the redline marks the median of the respective quantities, and the left and right whiskers represent the minimum and maximum of the observed changes, respectively.

The results in Fig. 9 b show that 82 % of LNAT is formed through the 'NC-to-LNAT' pathway, during which the corresponding air parcels are cooled (average ΔT = -0.75 K) as seen in Fig. 10a and led to the uptake of HNO₃ (average ΔHNO_3 = -0.8 ppbv) as seen in Fig. 10b. Though, according to CALIPSO PSC classification, NC refers to 'No Cloud' detected, it may yet contain either (i) stratospheric liquid sulfate aerosol immersed with foreign nuclei (such as meteoritic dust or smoke aerosols) or (ii) large NAT at very low number density, such that their optical signal is below the detection threshold of CALIPSO (Lambert et al., 2016). The former scenario leads to PSC formation through the uptake of HNO₃ (upon cooling of the air), and the latter leads to denitrification, which increases gas-phase HNO₃ (upon warming). Given an observed cooling and uptake of HNO₃, we consider that 'NC' primarily corresponds to the presence of stratospheric aerosols rather than large NAT. Furthermore, as stated earlier, the LNAT is a mixture of liquid STS and solid NAT (Pitts et al., 2011). The liquid STS can form through a homogeneous nucleation process from Stratospheric Sulfuric Acid (SSA; $H_2SO_4.H_2O$) which is ubiquitous in the stratosphere (Junge et al., 1961). As the temperature decreases, the SSA transforms into STS homogeneously, upon the uptake of H₂O and HNO₃ (Carslaw et al., 1994). Observational evidence based on ground-based lidar data supports the formation of STS through homogeneous nucleation (Biele et al., 2001). Hence, owing to the

observed decrease in temperature and gas-phase HNO_3, we primarily attribute the formation of liquid STS in the LNAT mixture to the homogeneous nucleation process.

Unlike STS, the homogeneous nucleation of NAT is kinetically suppressed (Koop et al., 1995). Thus, the

390 heterogeneous nucleation processes such as (i) ice-induced NAT nucleation and (ii) ice-free NAT nucleation are the possible ways of solid NAT formation. The former requires the presence of ice PSC which occurs only when the temperature $T-T_{ice} < 0$ (Carslaw et al., 1999). The latter requires the presence of solid foreign nuclei such as meteoritic dust, volcanic ash, soot, or H_2SO_4 hydrates which occurs even when the temperature is above $T-T_{ice}$ (Iraci et al., 1995; Peter and Grooß, 2012). We noticed that the majority of the LNAT is formed via the 'NC-to-

395 LNAT' pathway at temperatures $T-T_{ice} > 0$, averaging around $T-T_{ice} = 1.6$ K (Fig. 10c). Thus, the ice-free nucleation process is the primary cause of the observed LNAT formation rather than the ice-induced nucleation process, which is further substantiated by the observed uptake of HNO_3 and cooling of the air parcels.

We have observed that 15 % of the LNAT is formed through the 'Ice-to-LNAT' pathway (Fig. 9b), where the corresponding air parcels are found to be warming (average $\Delta T = 0.8$ K; Fig. 10a) and led to the release of HNO_3

400 (average $\Delta HNO_3 = 0.9$ ppbv; Fig. 10b). It occurred at a temperature of $T-T_{ice} = -0.9$ K (Fig. 10c). These observations rule out the possibility of heterogeneous nucleation of LNAT on ice, which occurs only after homogeneous nucleation of ice and requires $T-T_{ice} < -3$ K (Koop et al., 1995). Hence, the average ΔT and temperature at which LNAT is formed indicate that it is likely that the ice already nucleated on LNAT, and upon warming, the ice evaporated, leading to the exposure of the LNAT.

405 In the case of the 'STS-to-LNAT' pathway, which is responsible for 2.8 % of LNAT formation (Fig. 9b), the corresponding air parcels are found to be cooling (average $\Delta T = -0.7$ K) and resulted in condensation of HNO_3 (average $\Delta HNO_3 = -0.85$ ppbv) (Fig. 10a, b). Laboratory experiments have revealed that the homogeneous nucleation rate of NAT on STS is extremely low for stratospheric conditions (Hanson and Ravishankara, 1991; 1992). However, the STS, with the inclusion of foreign nuclei, can potentially serve as nuclei for NAT formation

410 (Koop et al., 1997). Ground-based lidar observations by Biele et al. (2001) provided evidence of the existence of such STS with foreign nuclei inclusion. As such, solid NAT would have nucleated on STS with foreign nuclei inclusion and thus transformed STS into LNAT mixture. A very meager fraction of the ENAT (~0.7 %) was transformed to LNAT and since there is no valid corresponding temperature data, the formation process is inconclusive.

415

3.5.2 Ice formation pathways
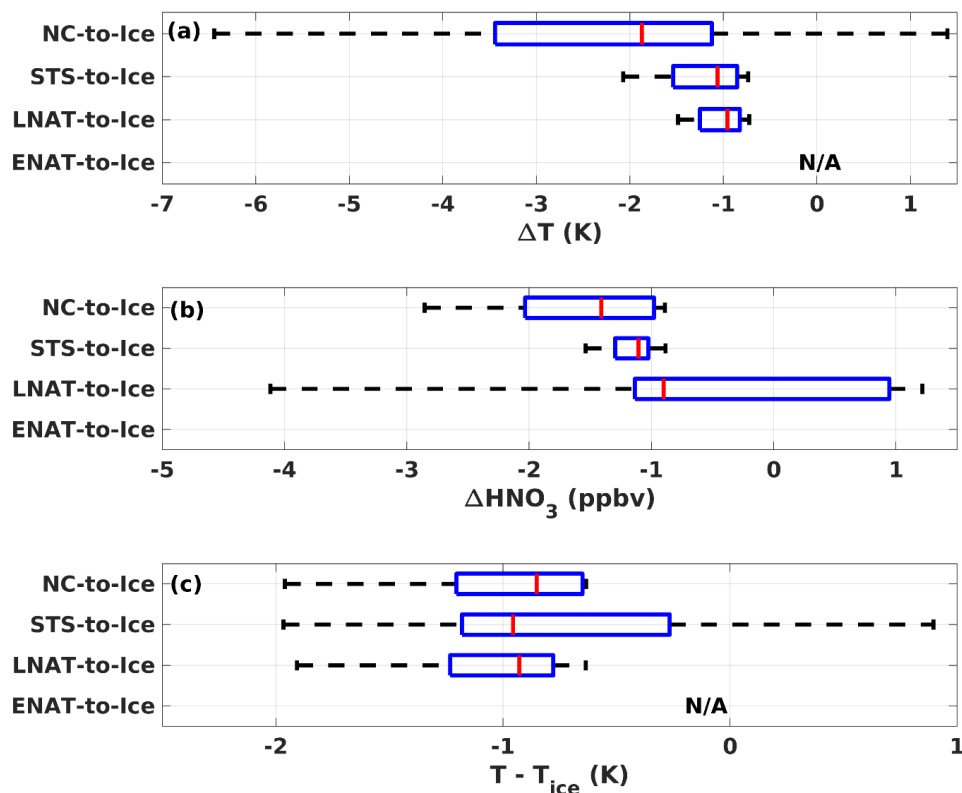
Figure 11: Same as Fig. 10 but for the case of ice PSC.

420   Figure 9d reveals that the most dominant formation pathway for ice formation is 'LNAT-to-Ice' (77 %), during which average ΔT is found to be -1 K, indicating cooling of the corresponding air parcels. The average ΔHNO_3 is found to be -0.9 ppbv, indicating an uptake of HNO_3 (Fig. 11 a, b). It occurred at the temperature of $T-T_{ice} = -0.95$ K (Fig. 11 c). The NAT is known to act as potential nuclei for ice formation (Khosrawi et al., 2011; Engel et al., 2013; Voigt et al., 2018). Hence, based on the observed change in temperature and the temperature at which

425   the ice formed, the ice nucleating on the existing LNAT is the most feasible pathway.

Following the LNAT-to-Ice pathway, 17 % of the ice is formed through the 'NC-to-Ice' pathway (Fig. 9d). During the ice formation through this pathway, a relatively rapid decrease in temperature, with an average ΔT of -1.9 K and a maximum cooling of -6.5 K, is observed (Fig. 11a). Furthermore, an uptake of HNO_3 with an average ΔHNO_3 of -1.4 ppbv is also observed (Fig. 11b). While homogeneous nucleation of ice is another possibility, it

430   occurs only under supercooled conditions at temperatures between $T-T_{ice} = -3$ K and $T-T_{ice} = -4$ K (Koop et al., 1998). But the observed temperature at which these ices are formed never fell below $T-T_{ice} = -2$ K, ruling out the possibility of homogeneous ice nucleation (Fig. 11c). It indicates that the 'NC-to-Ice' is possibly a tandem of two

pathways described above: 'NC-to-LNAT' and 'LNAT-to-Ice' (Peter, 1997). Due to the rapid temperature decrease, both these processes probably occurred in a relatively shorter time frame.
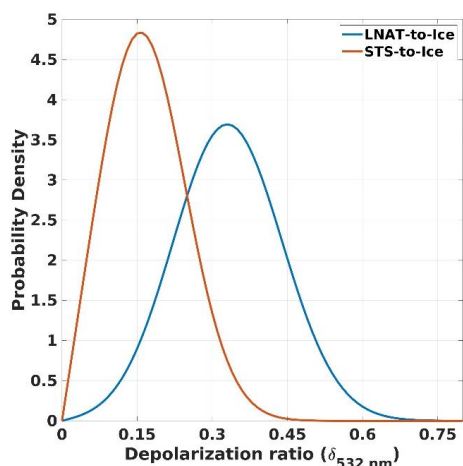
435

Figure 12: Probability density of the CALIPSO PSC depolarization ratio ($\delta_{532\ nm}$) for ice formed through the 'LNAT-to-Ice' pathway (blue line), and 'STS-to-Ice' pathway (orange line).

We observed just 5.1 % of the ice is formed through the 'STS-to-Ice" pathway (Fig. 9d). This process occurred at the temperature T-T$_{ice}$ = -0.95 K with an average ΔT and ΔHNO$_3$ of -0.7 K, and -0.9 ppbv respectively (Fig. 11a,

440 b). Similar to the 'STS-to-LNAT' pathway, the STS with solid nuclei inclusion could serve as nuclei for ice formation (Koop et al., 1998; 2000; Engel et al., 2013). The temperature at which this pathway has taken place indicates that the heterogeneous nucleation of ice on STS, with solid nuclei inclusion, could be a possible formation mechanism. Furthermore, we observed that the mean particulate depolarization ratio (δ_{532}) of ice nucleated on STS ('STS-to-Ice' pathway) is 0.15, which is less than half of the depolarization ratio of ice

445 (δ_{532}~0.36) nucleated on LNAT ('LNAT-to-Ice' pathway; Fig. 12). This observation is consistent with the results from a previous aircraft campaign conducted over Arctic PSC, where the authors showed that δ_{532} of ice PSC exhibited bimodal distribution and ice formed through the 'STS-to-Ice' pathway has relatively low δ_{532} compared to the ice formed through 'LNAT-to-Ice' pathway (Voigt et al., 2018). It is possible because STS is always in the liquid state and has a spherical shape, leading to low δ_{532}. Hence the ice nucleation on the STS is also likely to

450 lead to 'near-spherical' morphology. On the other hand, LNAT always exists in the solid state, and due to its non-spherical morphology, δ_{532} tends to be relatively larger than that of STS. The rest of the ice (2 %) is formed through the 'ENAT-to-Ice' pathway. Since there is no valid data for the corresponding thermodynamics parameters, further discussion on this is omitted.

From the above discussions, it is clear that the majority of the LNAT (82 %) and ice (77 %) are formed through

455 'NC-to-LNAT' and 'LNAT-to-Ice' pathways respectively. It indicates that LNAT nucleated on the stratospheric aerosols, which subsequently acted as nuclei for ice formation. Moreover, the 'LNAT-to-Ice' conversion should have occurred rapidly to explain the high anomalous ice areal coverage. In fact, both 'NC-to-LNAT' and 'LNAT-to-Ice' pathways are parts of the three-stage PSC formation model (Peter, 1997). During the first stage, the heterogeneously nucleated solid H$_2$SO$_4$ hydrates on other foreign nuclei such as meteoritic dust, soot, etc. present

460   in the atmosphere (Luo et al., 1994). Along with these nuclei, aerosols from the black summer event also participated in this stage during Austral winter 2020. In the second stage, these nuclei lead to heterogeneous nucleation of solid NAT, and in the third stage, upon cooling further, the ice nucleates on the pre-existing NAT (Peter, 1997; Lowe and MacKenzie, 2008). These results corroborate the hypothesis which we made earlier that majority of the Antarctic ice PSC forms by nucleating on the pre-existing NAT PSC.

465   In summary, we report the strong enhancement in aerosol loading in the lower stratosphere caused by the black summer event. In early 2020, it significantly affected the stratospheric chemistry by promoting increased production of HNO_3 at an altitude of ~25 km and directly injecting H_2O at an altitude of ~17 km. Subsequently, during Austral Winter 2020, anomalously high PSC areal coverage was observed, which conveys that the modified stratospheric chemistry strongly influenced the PSC formation. Furthermore, we observed that the ice areal

470   coverage exceeded three standard deviations with respect to the background mean while the LNAT remained within one standard deviation. To explain this behavior, we developed a novel methodology which retrieves the relative contribution of various PSC formation pathways from satellite measurements. The results revealed that most of the LNAT is formed via a heterogeneous nucleation process assisted by the aerosols from the black summer event. Subsequently, these LNAT rapidly acted as nuclei for ice formation, resulting in anomalous high

475   areal coverage of ice PSC. The consistency of the observed thermodynamics of the PSC formation process with our existing knowledge indicates that our methodology could efficiently retrieve the PSC formation pathways using satellite measurements. To the best of our knowledge, this is the first study which provides relative contributions of various LNAT and ice formation pathways. These results provide deeper insights into the microphysical processes through which the aerosols from extreme bushfire events (like black summer) can

480   influence the stratospheric chemistry and PSC formation.

4 Conclusions

Australia's extreme bushfire event of 2019/20, also referred to as black summer, injected 0.4 to 2 Tg of aerosols into the stratosphere, initiating a series of events. We carried out an extensive investigation on the impacts of bushfire emissions on the Polar Stratospheric Clouds (PSCs), using multi-satellite and reanalyses data. The key

485   findings from this study are:

1. During the austral autumn of 2020, we found a significant increase in gas phase nitric acid (HNO_3) and water vapor (H_2O) (principal constituents of PSCs) in high latitude region of the southern hemisphere at the altitudes of ~25 and ~17 km respectively. The former is due to the enhanced dinitrogen pentoxide hydrolysis process, caused by the increased bushfire aerosols. The latter is attributed to the direct injection of the water vapor by the black

490   summer event.

2. The increase in HNO_3 was expected to enhance HNO_3-containing PSCs like STS and NAT. While the areal coverage of STS peaked significantly, no notable enhancement in LNAT was observed. However, there was an anomalous increase in the areal coverage of ice PSC.

3. Most of the LNAT (~82 %) were formed through heterogeneous nucleation on bushfire aerosols. Consequently,

495   these LNAT served as nuclei for 77 % of ice PSC formation. This rapid conversion of LNAT to ice was responsible for the anomalous high areal coverage of ice PSC.

In the context of climate change scenarios, a warming troposphere and cooling stratosphere are anticipated. The former is expected to increase the frequency of extreme wildfire events and the latter is projected to enhance the PSC areal coverage, together possibly delaying the ozone recovery process. The findings from this study will contribute to a deeper understanding of the influence of extreme wildfire events on PSC dynamics.

Data availability

Processed data are available upon request.

Author contribution

SP conceived the work and carried out the scientific data analysis. SP, NSA, KS, KKM, and SKS were involved in the scientific interpretation of the results, leading to the formulation of the manuscript. SP prepared the initial draft with input from NSA. All authors reviewed the manuscript.

Competing interests

The authors declare that they have no conflict of interest.

Acknowledgements.

We acknowledge the mission scientists of OMPS (for aerosol extinction coefficient, and temperature), MLS (for HNO_3, and H_2O mixing ratio), ACE-FTS (for HNO_3, H_2O, HF, and N_2O_5 mixing ratio), ERA5 (for meteorological data), CALIPSO (for PSCs) and the associated personnel for the data used in this work. In addition, we acknowledge the CLaMS team for the model used in this work.

Financial support

One of the authors (SP) would like to thank the Centre for Research, Christ University for their support during this work. One of the authors (SKS) would like to thank SERB-DST for the J. C. Bose Fellowship. One of the authors (NSA) is supported by the DST in the form of an INSPIRE Faculty Fellowship (faculty registration number: IFA20-EAS-83). We thank the Divecha Centre for Climate Change for supporting this work.

References

Allen, D. R., Fromm, M. D., Kablick III, G. P., and Nedoluha, G. E.: Smoke with induced rotation and lofting (SWIRL) in the stratosphere, J Atmos Sci, 77, 4297–4316, 2020.

Ansmann, A., Ohneiser, K., Chudnovsky, A., Knopf, D. A., Eloranta, E. W., Villanueva, D., Seifert, P., Radenz, M., Barja, B., Zamorano, F., Jimenez, C., Engelmann, R., Baars, H., Griesche, H., Hofer, J., Althausen, D., and Wandinger, U.: Ozone depletion in the Arctic and Antarctic stratosphere induced by wildfire smoke, Atmos Chem Phys, 22, 11701–11726, https://doi.org/10.5194/ACP-22-11701-2022, 2022.

Bell, S. A.: A beginner's guide to uncertainty of measurement., 2nd ed., National Physical Laboratory Teddington, Middlesex, United Kingdom, 2001.

Bernath, P. F., Steffen, J., Crouse, J., and Boone, C. D.: Atmospheric Chemistry Experiment SciSat Level 2 Processed Data, v4.0, 2020.

Biele, J., Tsias, A., Luo, B. P., Carslaw, K. S., Neuber, R., Beyerle, G., and Peter, T.: Nonequilibrium coexistence of solid and liquid particles in Arctic stratospheric clouds, Journal of Geophysical Research: Atmospheres, 106, 22991–23007, https://doi.org/10.1029/2001JD900188, 2001.

535   Brewer, A. W.: Evidence for a world circulation provided by the measurements of helium and water vapour distribution in the stratosphere, Quarterly Journal of the Royal Meteorological Society, 75, 351–363, https://doi.org/10.1002/QJ.49707532603, 1949.

Butchart, N.: The Brewer-Dobson circulation, Reviews of Geophysics, 52, 157–184, https://doi.org/10.1002/2013RG000448, 2014.

Carslaw, K. S., Luo, B. P., Clegg, S. L., Peter, T., Brimblecombe, P., and Crutzen, P. J.: Stratospheric aerosol
540   growth and HNO3 gas phase depletion from coupled HNO3 and water uptake by liquid particles, Geophys Res Lett, 21, 2479–2482, https://doi.org/10.1029/94GL02799, 1994.

Carslaw, K. S., Peter, T., Bacmeister, J. T., and Eckermann, S. D.: Widespread solid particle formation by mountain waves in the Arctic stratosphere, Journal of Geophysical Research: Atmospheres, 104, 1827–1836, https://doi.org/10.1029/1998JD100033, 1999.

545   Chang, D. Y., Yoon, J., Lelieveld, J., Park, S. K., Yum, S. S., Kim, J., and Jeong, S.: Direct radiative forcing of biomass burning aerosols from the extensive Australian wildfires in 2019–2020, Environmental Research Letters, 16, 044041, https://doi.org/10.1088/1748-9326/ABECFE, 2021.

Deb, P., Moradkhani, H., Abbaszadeh, P., Kiem, A. S., Engström, J., Keellings, D., and Sharma, A.: Causes of the Widespread 2019–2020 Australian Bushfire Season, Earths Future, 8, e2020EF001671,
550   https://doi.org/https://doi.org/10.1029/2020EF001671, 2020.

Engel, I., Luo, B. P., Pitts, M. C., Poole, L. R., Hoyle, C. R., Grooß, J. U., Dörnbrack, A., and Peter, T.: Heterogeneous formation of polar stratospheric clouds-Part 2: Nucleation of ice on synoptic scales, Atmos Chem Phys, 13, 10769–10785, https://doi.org/10.5194/ACP-13-10769-2013, 2013.

Fueglistaler, S., Dessler, A. E., Dunkerton, T. J., Folkins, I., Fu, Q., and Mote, P. W.: Tropical tropopause layer,
555   Reviews of Geophysics, 47, https://doi.org/10.1029/2008RG000267, 2009.

Graham, R. M., Hudson, S. R., and Maturilli, M.: Improved Performance of ERA5 in Arctic Gateway Relative to Four Global Atmospheric Reanalyses, Geophys Res Lett, 46, 6138–6147, https://doi.org/10.1029/2019GL082781, 2019.

Hamill, P. and Mcmaster, L. R.: Proceedings of a Workshop on Polar Stratospheric Clouds: Their Role in
560   Atmospheric Processes, 1984.

Hanson, D. R. and Ravishankara, A. R.: The reaction probabilities of ClONO2 and N2O5 on 40 to 75% sulfuric acid solutions, Journal of Geophysical Research: Atmospheres, 96, 17307–17314, https://doi.org/10.1029/91JD01750, 1991.

Hanson, D. R. and Ravishankara, A. R.: Investigation of the reactive and nonreactive processes involving nitryl
565   hypochlorite and hydrogen chloride on water and nitric acid doped ice, J Phys Chem, 96, 2682–2691, 1992.

Heinold, B., Baars, H., Barja, B., Christensen, M., Kubin, A., Ohneiser, K., Schepanski, K., Schutgens, N., Senf, F., and Schrödner, R.: Important role of stratospheric injection height for the distribution and radiative forcing of smoke aerosol from the 2019/2020 Australian wildfires, Atmospheric Chemistry and Physics Discussions, 1–20, 2021.

570   Hersbach, H., Bell, B., Berrisford, P., Hirahara, S., Horányi, A., Muñoz-Sabater, J., Nicolas, J., Peubey, C., Radu, R., Schepers, D., Simmons, A., Soci, C., Abdalla, S., Abellan, X., Balsamo, G., Bechtold, P., Biavati, G., Bidlot, J., Bonavita, M., De Chiara, G., Dahlgren, P., Dee, D., Diamantakis, M., Dragani, R., Flemming, J., Forbes, R., Fuentes, M., Geer, A., Haimberger, L., Healy, S., Hogan, R. J., Hólm, E., Janisková, M., Keeley, S., Laloyaux, P., Lopez, P., Lupu, C., Radnoti, G., de Rosnay, P., Rozum, I., Vamborg, F.,
575   Villaume, S., and Thépaut, J. N.: The ERA5 global reanalysis, Quarterly Journal of the Royal Meteorological Society, 146, 1999–2049, https://doi.org/10.1002/QJ.3803, 2020.

Hirsch, E. and Koren, I.: Record-breaking aerosol levels explained by smoke injection into the stratosphere, Science (1979), 371, 1269–1274, 2021.

580   Hoyle, C. R., Engel, I., Luo, B. P., Pitts, M. C., Poole, L. R., Grooß, J. U., and Peter, T.: Heterogeneous formation of polar stratospheric clouds-Part 1: Nucleation of nitric acid trihydrate (NAT), Atmos Chem Phys, 13, 9577–9595, https://doi.org/10.5194/ACP-13-9577-2013, 2013.

Huff, D.: How to lie with statistics, Penguin UK, 2023.

Iraci, L. T., Middlebrook, A. M., and Tolbert, M. A.: Laboratory studies of the formation of polar stratospheric clouds: Nitric acid condensation on thin sulfuric acid films, Journal of Geophysical Research: Atmospheres, 100, 20969–20977, https://doi.org/10.1029/95JD02267, 1995.

Junge, C. E., Chagnon, C. W., and Manson, J. E.: STRATOSPHERIC AEROSOLS, Journal of Atmospheric Sciences, 18, 81–108, https://doi.org/https://doi.org/10.1175/1520-0469(1961)018<0081:SA>2.0.CO;2, 1961.

590   Kessenich, H. E., Seppälä, A., and Rodger, C. J.: Potential drivers of the recent large Antarctic ozone holes, Nature Communications 2023 14:1, 14, 1–9, https://doi.org/10.1038/s41467-023-42637-0, 2023.

Khaykin, S., Legras, B., Bucci, S., Sellitto, P., Isaksen, L., Tence, F., Bekki, S., Bourassa, A., Rieger, L., and Zawada, D.: The 2019/20 Australian wildfires generated a persistent smoke-charged vortex rising up to 35 km altitude, Commun Earth Environ, 1, 1–12, 2020.

595   Khosrawi, F., Urban, J., Pitts, M. C., Voelger, P., Achtert, P., Kaphlanov, M., Santee, M. L., Manney, G. L., Murtagh, D., and Fricke, K. H.: Denitrification and polar stratospheric cloud formation during the Arctic winter 2009/2010, Atmos Chem Phys, 11, 8471–8487, https://doi.org/10.5194/ACP-11-8471-2011, 2011.

Koop, T., Biermann, U. M., Raber, W., Luo, B. P., Crutzen, P. J., and Peter, T.: Do stratospheric aerosol droplets freeze above the ice frost point?, Geophys Res Lett, 22, 917–920, https://doi.org/10.1029/95GL00814, 1995.

600   Koop, T., Luo, B., Biermann, U. M., Crutzen, P. J., and Peter, T.: Freezing of HNO3/H2SO4/H2O Solutions at Stratospheric Temperatures: Nucleation Statistics and Experiments, J Phys Chem A, 101, 1117–1133, https://doi.org/10.1021/jp9626531, 1997.

Koop, T., Ng, H. P., Molina, L. T., and Molina, M. J.: A New Optical Technique to Study Aerosol Phase Transitions: The Nucleation of Ice from H2SO4 Aerosols, J Phys Chem A, 102, 8924–8931, 605   https://doi.org/10.1021/jp9828078, 1998.

Koop, T., Luo, B., Tsias, A., and Peter, T.: Water activity as the determinant for homogeneous ice nucleation in aqueous solutions, Nature 2000 406:6796, 406, 611–614, https://doi.org/10.1038/35020537, 2000.

Lambert, A., Santee, M. L., Wu, D. L., and Chae, J. H.: A-train CALIOP and MLS observations of early winter Antarctic polar stratospheric clouds and nitric acid in 2008, Atmos Chem Phys, 12, 2899–2931, 610   https://doi.org/10.5194/ACP-12-2899-2012, 2012.

Lambert, A., Santee, M. L., and Livesey, N. J.: Interannual variations of early winter Antarctic polar stratospheric cloud formation and nitric acid observed by CALIOP and MLS, Atmos Chem Phys, 16, 15219–15246, https://doi.org/10.5194/ACP-16-15219-2016, 2016.

Li, M., Shen, F., and Sun, X.: 2019–2020 Australian bushfire air particulate pollution and impact on the South 615   Pacific Ocean, Scientific Reports 2021 11:1, 11, 1–13, https://doi.org/10.1038/s41598-021-91547-y, 2021.

Liu, G., Hirooka, T., Eguchi, N., and Krüger, K.: Dynamical evolution of a minor sudden stratospheric warming in the Southern Hemisphere in 2019, Atmos Chem Phys, 22, 3493–3505, https://doi.org/10.5194/ACP-22-3493-2022, 2022.

Lowe, D. and MacKenzie, A. R.: Polar stratospheric cloud microphysics and chemistry, J Atmos Sol Terr Phys, 620   70, 13–40, https://doi.org/10.1016/J.JASTP.2007.09.011, 2008.

Luo, B., Peter, T., and Crutzen, P.: Freezing of stratospheric aerosol droplets, Geophys Res Lett, 21, 1447–1450, https://doi.org/10.1029/93GL03076, 1994.

Mansoor, S., Farooq, I., Kachroo, M. M., Mahmoud, A. E. D., Fawzy, M., Popescu, S. M., Alyemeni, M. N., Sonne, C., Rinklebe, J., and Ahmad, P.: Elevation in wildfire frequencies with respect to the climate change, J Environ Manage, 301, 113769, https://doi.org/10.1016/J.JENVMAN.2021.113769, 2022.

Molina, M. J., Zhang, R., Wooldridge, P. J., McMahon, J. R., Kim, J. E., Chang, H. Y., and Beyer, K. D.: Physical chemistry of the H2SO4/HNO 3/H2O system: Implications for polar stratospheric clouds, Science (1979), 261, 1418–1423, https://doi.org/10.1126/SCIENCE.261.5127.1418, 1993.

Müller, R., Crutzen, P. J., Grooß, J.-U., Brühl, C., Russell III, J. M., and Tuck, A. F.: Chlorine activation and ozone depletion in the Arctic vortex: Observations by the Halogen Occultation Experiment on the Upper Atmosphere Research Satellite, Journal of Geophysical Research: Atmospheres, 101, 12531–12554, https://doi.org/https://doi.org/10.1029/95JD00220, 1996.

Müller, R., Crutzen, P. J., Grooβ, J.-U., Bürhl, C., Russell, J. M., Gernandt, H., McKenna, D. S., and Tuck, A. F.: Severe chemical ozone loss in the Arctic during the winter of 1995–96, Nature, 389, 709–712, https://doi.org/10.1038/39564, 1997.

Murphy, D. M. and Koop, T.: Review of the vapour pressures of ice and supercooled water for atmospheric applications, Quarterly Journal of the Royal Meteorological Society, 131, 1539–1565, https://doi.org/10.1256/QJ.04.94, 2005.

Nakajima, H., Wohltmann, I., Wegner, T., Takeda, M., Pitts, M. C., Poole, L. R., Lehmann, R., Santee, M. L., and Rex, M.: Polar stratospheric cloud evolution and chlorine activation measured by CALIPSO and MLS, and modeled by ATLAS, Atmos Chem Phys, 16, 3311–3325, https://doi.org/10.5194/ACP-16-3311-2016, 2016.

Ohneiser, K., Ansmann, A., Kaifler, B., Chudnovsky, A., Barja, B., Knopf, D. A., Kaifler, N., Baars, H., Seifert, P., Villanueva, D., Jimenez, C., Radenz, M., Engelmann, R., Veselovskii, I., and Zamorano, F.: Australian wildfire smoke in the stratosphere: the decay phase in 2020/2021 and impact on ozone depletion, Atmos. Chem. Phys., 22, 7417–7442, https://doi.org/10.5194/acp-22-7417-2022, 2022.

Peter, T.: MICROPHYSICS AND HETEROGENEOUS CHEMISTRY OF POLAR STRATOSPHERIC CLOUDS, https://doi.org/10.1146/annurev.physchem.48.1.785, 48, 785–822, https://doi.org/10.1146/ANNUREV.PHYSCHEM.48.1.785, 1997.

Peter, T. and Grooß, J.-U.: Stratospheric ozone depletion and climate change, Royal Society of Chemistry, 108–144 pp., 2012.

Pitts, M. C., Thomason, L. W., Poole, L. R., and Winker, D. M.: Characterization of polar stratospheric clouds with spaceborne lidar: CALIPSO and the 2006 antarctic season, Atmos Chem Phys, 7, 5207–5228, https://doi.org/10.5194/ACP-7-5207-2007, 2007.

Pitts, M. C., Poole, L. R., and Thomason, L. W.: CALIPSO polar stratospheric cloud observations: Second-generation detection algorithm and composition discrimination, Atmos Chem Phys, 9, 7577–7589, https://doi.org/10.5194/ACP-9-7577-2009, 2009.

Pitts, M. C., Poole, L. R., Därnbrack, A., and Thomason, L. W.: The 2009-2010 Arctic polar stratospheric cloud season: A CALIPSO perspective, Atmos Chem Phys, 11, 2161–2177, https://doi.org/10.5194/ACP-11-2161-2011, 2011.

Pitts, M. C., Poole, L. R., Lambert, A., and Thomason, L. W.: An assessment of CALIOP polar stratospheric cloud composition classification, Atmos Chem Phys, 13, 2975–2988, https://doi.org/10.5194/ACP-13-2975-2013, 2013.

Ravishankara, A. R. and Hanson, D. R.: Differences in the reactivity of type I polar stratospheric clouds depending on their phase, Journal of Geophysical Research: Atmospheres, 101, 3885–3890, https://doi.org/10.1029/95JD03009, 1996.

Rex, M., Salawitch, R. J., von der Gathen, P., Harris, N. R. P., Chipperfield, M. P., and Naujokat, B.: Arctic ozone loss and climate change, Geophys Res Lett, 31, 2004.

670   Rieger, L. A., Randel, W. J., Bourassa, A. E., and Solomon, S.: Stratospheric temperature and ozone anomalies associated with the 2020 Australian New Year Fires, Geophys Res Lett, 48, e2021GL095898, 2021.

Robrecht, S., Vogel, B., Grooß, J. U., Rosenlof, K., Thornberry, T., Rollins, A., Krämer, M., Christensen, L., and Müller, R.: Mechanism of ozone loss under enhanced water vapour conditions in the mid-latitude lower stratosphere in summer, Atmos Chem Phys, 19, 5805–5833, https://doi.org/10.5194/ACP-19-5805-2019, 2019.

675   Santee, M. L., Lambert, A., Manney, G. L., Livesey, N. J., Froidevaux, L., Neu, J. L., Schwartz, M. J., Millán, L. F., Werner, F., Read, W. G., Park, M., Fuller, R. A., and Ward, B. M.: Prolonged and Pervasive Perturbations in the Composition of the Southern Hemisphere Midlatitude Lower Stratosphere From the Australian New Year's Fires, Geophys Res Lett, 49, e2021GL096270, https://doi.org/10.1029/2021GL096270, 2022.

680   Schoeberl, M. R., Jensen, E. J., Pfister, L., Ueyama, R., Avery, M., and Dessler, A. E.: Convective Hydration of the Upper Troposphere and Lower Stratosphere, Journal of Geophysical Research: Atmospheres, 123, 4583–4593, https://doi.org/10.1029/2018JD028286, 2018.

Schwartz, M. J., Santee, M. L., Pumphrey, H. C., Manney, G. L., Lambert, A., Livesey, N. J., Millán, L., Neu, J. L., Read, W. G., and Werner, F.: Australian new year's pyrocb impact on stratospheric composition,
685   Geophys Res Lett, 47, e2020GL090831, 2020.

Sellitto, P., Belhadji, R., Kloss, C., and Legras, B.: Radiative impacts of the Australian bushfires 2019–2020–Part 1: Large-scale radiative forcing, EGUsphere, 1–20, 2022.

Solomon, S., Dube, K., Stone, K., Yu, P., Kinnison, D., Toon, O. B., Strahan, S. E., Rosenlof, K. H., Portmann, R., Davis, S., Randel, W., Bernath, P., Boone, C., Bardeen, C. G., Bourassa, A., Zawada, D., and
690   Degenstein, D.: On the stratospheric chemistry of midlatitude wildfire smoke, Proc Natl Acad Sci U S A, 119, e2117325119, https://doi.org/10.1073/PNAS.2117325119/SUPPL_FILE/PNAS.2117325119.SAPP.PDF, 2022.

Stocker, M., Ladstädter, F., and Steiner, A. K.: Observing the climate impact of large wildfires on stratospheric temperature, Sci Rep, 11, 22994, https://doi.org/10.1038/s41598-021-02335-7, 2021.

695   Taha, G., Loughman, R., Zhu, T., Thomason, L., Kar, J., Rieger, L., and Bourassa, A.: OMPS LP Version 2.0 multi-wavelength aerosol extinction coefficient retrieval algorithm, Atmos Meas Tech, 14, 1015–1036, https://doi.org/10.5194/AMT-14-1015-2021, 2021.

Tencé, F., Jumelet, J., Sarkissian, A., Bekki, S., and Khaykin, S.: Optical properties of smoke particles from Australian 2019-20 wildfires derived from lidar measurements at the French Antarctic station Dumont
700   d'Urville, in: EGU General Assembly Conference Abstracts, EGU21-12466, 2021.

Tencé, F., Jumelet, J., Bekki, S., Khaykin, S., Sarkissian, A., and Keckhut, P.: Australian Black Summer Smoke Observed by Lidar at the French Antarctic Station Dumont d'Urville, Journal of Geophysical Research: Atmospheres, 127, e2021JD035349, https://doi.org/10.1029/2021JD035349, 2022.

Toon, O. B., Turco, R. P., Jordan, J., Goodman, J., and Ferry, G.: Physical processes in polar stratospheric ice
705   clouds, Journal of Geophysical Research: Atmospheres, 94, 11359–11380, 1989.

Tritscher, I., Pitts, M. C., Poole, L. R., Alexander, S. P., Cairo, F., Chipperfield, M. P., Grooß, J. U., Höpfner, M., Lambert, A., Luo, B., Molleker, S., Orr, A., Salawitch, R., Snels, M., Spang, R., Woiwode, W., and Peter, T.: Polar Stratospheric Clouds: Satellite Observations, Processes, and Role in Ozone Depletion, Reviews of Geophysics, 59, e2020RG000702, https://doi.org/10.1029/2020RG000702, 2021.

710   Voigt, C., Dörnbrack, A., Wirth, M., Groß, S. M., Pitts, M. C., Poole, L. R., Baumann, R., Ehard, B., Sinnhuber, B. M., Woiwode, W., and Oelhaf, H.: Widespread polar stratospheric ice clouds in the 2015-2016 Arctic winter - Implications for ice nucleation, Atmos Chem Phys, 18, 15623–15641, https://doi.org/10.5194/ACP-18-15623-2018, 2018.

Wang, P., Solomon, S., and Stone, K.: Stratospheric chlorine processing after the 2020 Australian wildfires derived from satellite data, Proc Natl Acad Sci U S A, 120, e2213910120, https://doi.org/10.1073/PNAS.2213910120/SUPPL_FILE/PNAS.2213910120.SAPP.PDF, 2023.

Yu, P., Davis, S. M., Toon, O. B., Portmann, R. W., Bardeen, C. G., Barnes, J. E., Telg, H., Maloney, C., and Rosenlof, K. H.: Persistent stratospheric warming due to 2019–2020 Australian wildfire smoke, Geophys Res Lett, 48, e2021GL092609, 2021.

Zhang, R., Leu, M., and Keyser, L. F.: Hydrolysis of N2O5 and ClONO2 on the H2SO4/HNO3/H2O ternary solutions under stratospheric conditions, Geophys Res Lett, 22, 1493–1496, 1995.

Zhu, Y., Toon, O. B., Kinnison, D., Harvey, V. L., Mills, M. J., Bardeen, C. G., Pitts, M., Bègue, N., Renard, J. B., Berthet, G., and Jégou, F.: Stratospheric Aerosols, Polar Stratospheric Clouds, and Polar Ozone Depletion After the Mount Calbuco Eruption in 2015, Journal of Geophysical Research: Atmospheres, 123, 12,308-12,331, https://doi.org/10.1029/2018JD028974, 2018.